

# ADAPTIVELY REFINED LARGE EDDY SIMULATIONS OF A GALAXY CLUSTER: TURBULENCE MODELING AND THE PHYSICS OF THE INTRA-CLUSTER MEDIUM

A. MAIER<sup>1</sup>, L. IAPICHINO<sup>2</sup>, W. SCHMIDT<sup>1</sup> AND J.C. NIEMEYER<sup>3</sup>

*Draft version November 8, 2018*

## ABSTRACT

We present a numerical scheme for modelling unresolved turbulence in cosmological adaptive mesh refinement codes. As a first application, we study the evolution of turbulence in the intra-cluster medium and in the core of a galaxy cluster. Simulations with and without subgrid scale model are compared in detail. Since the flow in the ICM is subsonic, the global turbulent energy contribution at the unresolved length scales is smaller than 1% of the internal energy. We find that the production of turbulence is closely correlated with merger events occurring in the cluster environment, and its dissipation locally affects the cluster energy budget. Because of this additional source of dissipation, the core temperature is larger and the density is smaller in the presence of subgrid scale turbulence than in the standard adiabatic run, resulting in a higher entropy core value.

*Subject headings:* galaxies: clusters: general — hydrodynamics — methods: numerical — turbulence

## 1. INTRODUCTION

Simulations of cosmological structure formation often share two important attributes. First, the ubiquitous presence of spatially localized features such as shocks, clumps, or composition discontinuities that need to be numerically resolved or at least adequately modeled; and second, moderate or large Reynolds numbers of the baryonic component indicating that fully developed, i.e. space-filling turbulence is responsible for the mixing and dissipation properties of the gas. Despite great advances in computational fluid dynamics, an accurate handling of both aspects has so far proven to be very difficult, because dedicated numerical techniques seem to be mutually incompatible.

The most powerful technique for grid-based solvers to resolve localized and anisotropic structures in a flow is adaptive mesh refinement (AMR) (Berger & Olinger 1984; Berger & Colella 1989). This technique has proven to be very well suited for several astrophysical problems (Norman 2005). However, in the case of astrophysically relevant Reynolds numbers even with AMR we cannot resolve all the relevant length scales down to the dissipative one (Schmidt et al. 2006). Even if this condition may be achieved in regions of maximum refinement, as is possibly the case in the core of galaxy clusters (where the effective viscosity is still the subject of debate), turbulence from coarser areas of the grid continuously flows into these regions without being properly accounted for.

In engineering applications as well as other fields of computational fluid dynamics, subgrid scale (SGS) models have been developed in order to mimic the influence of unresolved turbulence on the resolved scales. This technique is often referred to as Large Eddy Simulations (LES) (Lesieur & Metais 1996). In astrophysics, SGS models have already been exten-

sively used in simulations of Type Ia supernova explosions (Niemeyer & Hillebrandt 1995; Reinecke et al. 2002; Röpke & Hillebrandt 2005; Röpke et al. 2007). In this framework, Schmidt et al. (2006) presented a formulation of SGS models based on the filtering approach of Germano (1992). Other applications of SGS models in astrophysical problems have been proposed by Pope et al. (2008) and, in an approach specially designed for Rayleigh-Taylor-driven turbulence, by Scannapieco & Brügggen (2008).

In this paper, a numerical method that combines LES and AMR for the study of astrophysical turbulent flows will be presented. We will refer to this new tool as FEARLESS (Fluid mEchanics with Adaptively Refined Large Eddy SimulationS). With the combined use of grid refinement and SGS model, FEARLESS is very suitable for simulations of intermittent turbulent flows in clumped media.

The formation and evolution of the cosmological large scale structure is a typical case of turbulence generation in a strongly clumped medium. The concordance model of cosmological structure formation explains the formation of clusters through a hierarchical sequence of mergers of lower-mass systems (e.g. Ostriker 1993). In particular, mergers of subhalos play a fundamental role in determining the structure and dynamics of massive clusters of galaxies. Furthermore, it is known that major mergers induce temperature inhomogeneities and bulk motions with velocities of the order of  $1000 \text{ km s}^{-1}$  in the intra-cluster medium (ICM) (Norman & Bryan 1999). This results in complex hydrodynamic flows where most of the kinetic energy is quickly dissipated to heat by shocks, but some part may in principle also excite long-lasting turbulent gas motions. Besides merger processes, it is also known that galactic motions (Bregman & David 1989; Kim 2007) and AGN outflows (Heinz et al. 2006; Sijacki & Springel 2006) can stir the ICM.

The problem of the turbulent state of the ICM is still controversial, both from the theoretical point of view of constraining the kinematic viscosity of the fluid (Reynolds et al. 2005; Narayan & Medvedev 2001; Jones 2008), and from the observational side, since a direct ob-

arXiv:0909.1800v3 [astro-ph.CO] 10 Sep 2009

<sup>1</sup> Lehrstuhl für Astronomie, Universität Würzburg, Am Hubland, D-97074 Würzburg, Germany

<sup>2</sup> Zentrum für Astronomie der Universität Heidelberg, Institut für Theoretische Astrophysik, Albert-Ueberle-Str 2, D-69120 Heidelberg, Germany

<sup>3</sup> Institut für Astrophysik, Universität Göttingen, Friedrich-Hund-Platz 1, D-37077 Göttingen, Germany

servation of turbulent emission-line broadening is beyond the reach of current X-ray observatories (Sunyaev et al. 2003; Inogamov & Sunyaev 2003; Brügggen et al. 2005; Dolag et al. 2005; Rebusco et al. 2008). Nonetheless, some indirect ways of investigating turbulence in clusters gave encouraging results (see Iapichino & Niemeyer 2008 for an overview) and call for a better theoretical understanding of the problem. A clear example for the relevance of cluster turbulence for precision cosmology is provided by recent results that demonstrate the sensitivity of hydrostatic mass estimates on assumptions about the level of turbulence (Lau et al. 2009).

In numerical simulations of merging clusters (Schindler & Mueller 1993; Roettiger et al. 1997; Ricker & Sarazin 2001; Fujita et al. 2004a,b; Takizawa 2005a; Iapichino et al. 2008), it has been shown that infalling subclusters generate a laminar bulk flow but inject turbulent motions via Kelvin-Helmholtz instabilities at the interfaces between the bulk flows and the primary cluster gas. Such eddies redistribute the energy of the merger through the cluster volume and decay into turbulent velocity fields, eventually developing a turbulent cascade with a spectrum of fluctuations expected to be close to a Kolmogorov spectrum (Dolag et al. 2005). Numerical simulations focused on the role of turbulence in astrophysical flows in general, and especially for clusters, have been restricted to measuring passively statistical quantities like velocity dispersion from simulation data (e.g. Norman & Bryan 1999; Dolag et al. 2005). The active role of small scale velocity fluctuations on the large scale flow has not been taken into account so far.

A previous attempt of modelling turbulence in hydrodynamical simulation of cluster formation has been performed by Iapichino & Niemeyer (2008). In that work, the authors focused on better definitions of the AMR criteria for refining the computational grid where and when the flow in the ICM was turbulent (Schmidt et al. 2009; Iapichino et al. 2008). Though useful, this numerical strategy can follow only a narrow range of large length scales along the turbulent cascade, being the Kolmogorov length scale for turbulent dissipation much lower than the spatial resolution. Besides this theoretical shortcoming, also numerically it is questionable whether the mixing forced at the mesh length scale correctly represents the physics of turbulence (Mitchell et al. 2009).

These arguments motivate the application of FEARLESS to cluster simulations as a more consistent approach. We show below that the additional degree of freedom given by the local turbulence intensity on unresolved scales has a measurable impact on the features of the ICM. In addition to the direct dynamical coupling to the resolved fluid equations, the ability to separate unresolved kinetic energy from thermal energy allows a more accurate computation of the local temperature and entropy than without the subgrid scale model.

This work is structured as follows: in §2, the formalism of the subgrid scale model and of FEARLESS is introduced. Some numerical tests and consistency checks are presented in §3, and the setup of the galaxy cluster simulations is described in §4. The results are presented in §5 and discussed in §6, where our conclusions are drawn.

## 2. SUBGRID SCALE MODEL AND FEARLESS

### 2.1. Germano decomposition

The dynamics of a compressible, viscous, self-gravitating fluid with density  $\rho(r_i, t)$ , momentum density  $\rho v_i(r_i, t)$  and total energy density  $\rho e(r_i, t)$  at spatial position  $(r_1, r_2, r_3)$  is given by the following set of equations:

$$\frac{\partial}{\partial t} \rho + \frac{\partial}{\partial r_j} (v_j \rho) = 0, \quad (1)$$

$$\frac{\partial}{\partial t} (\rho v_i) + \frac{\partial}{\partial r_j} (v_j \rho v_i) = - \frac{\partial}{\partial r_i} p + \frac{\partial}{\partial r_j} \sigma'_{ij} + \rho g_i, \quad (2)$$

$$\frac{\partial}{\partial t} (\rho e) + \frac{\partial}{\partial r_j} (v_j \rho e) = - \frac{\partial}{\partial r_j} (v_j p) + \frac{\partial}{\partial r_j} (v_i \sigma'_{ij}) + v_i \rho g_i, \quad (3)$$

where  $p$  is the pressure,  $g_i$  the gravitational acceleration and  $\sigma'_{ij}$  the viscous stress tensor. Note that the Einstein sum convention applies to repeated indices.

As shown by Schmidt et al. (2006), these equations can be decomposed into large-scale (resolved) and small-scale (unresolved) parts using the filter formalism proposed by Germano (1992) in terms of density-weighted quantities<sup>4</sup>. By means of filtering, any field quantity  $a$  can be split into a smoothed part  $\langle a \rangle$  and a fluctuating part  $a'$ , where  $\langle a \rangle$  varies only at scales greater than the prescribed filter length. We define density weighted filtered quantities according to Favre (1969) by

$$\langle \rho a \rangle = \langle \rho \rangle \hat{a} \Rightarrow \hat{a} = \frac{\langle \rho a \rangle}{\langle \rho \rangle}. \quad (4)$$

Following Schmidt et al. (2006), filtered equations for compressible fluid dynamics can be derived:

$$\frac{\partial}{\partial t} \langle \rho \rangle + \frac{\partial}{\partial r_j} \hat{v}_j \langle \rho \rangle = 0, \quad (5)$$

$$\begin{aligned} \frac{\partial}{\partial t} \langle \rho \rangle \hat{v}_i + \frac{\partial}{\partial r_j} \hat{v}_j \langle \rho \rangle \hat{v}_i = & - \frac{\partial}{\partial r_i} \langle p \rangle + \frac{\partial}{\partial r_j} \langle \sigma'_{ij} \rangle \\ & + \langle \rho \rangle \hat{g}_i - \frac{\partial}{\partial r_j} \hat{\tau}(v_i, v_j), \end{aligned} \quad (6)$$

$$\begin{aligned} \frac{\partial}{\partial t} \langle \rho \rangle e_{\text{res}} + \frac{\partial}{\partial r_j} \hat{v}_j \langle \rho \rangle e_{\text{res}} = & - \frac{\partial}{\partial r_i} \hat{v}_i \langle p \rangle + \frac{\partial}{\partial r_j} \hat{v}_i \langle \sigma'_{ij} \rangle \\ & + \langle \rho \rangle (\lambda + \epsilon) - \hat{v}_i \frac{\partial}{\partial r_j} \hat{\tau}(v_i, v_j) \\ & + \langle \rho \rangle \hat{v}_i \hat{g}_i - \frac{\partial}{\partial r_j} \hat{\tau}(v_j, e_{\text{int}}), \end{aligned} \quad (7)$$

where we introduced the total resolved energy  $e_{\text{res}} = \hat{e}_{\text{int}} + \frac{1}{2} \hat{v}_i \hat{v}_i$ , being  $\hat{e}_{\text{int}}$  the filtered internal energy, and the generalized moments which are generically defined by

$$\hat{\tau}(a, b) = \langle \rho a b \rangle - \langle \rho \rangle \hat{a} \hat{b} \quad (8)$$

$$\begin{aligned} \hat{\tau}(a, b, c) = & \langle \rho a b c \rangle - \langle \rho \rangle \hat{a} \hat{b} \hat{c} \\ & - \hat{a} \hat{\tau}(b, c) - \hat{b} \hat{\tau}(a, c) - \hat{c} \hat{\tau}(a, b) \end{aligned} \quad (9)$$

$$\hat{\tau}(a, b, c, d) = \dots \quad (10)$$

for Favre-filtered quantities  $a, b, c$  etc. Germano interpreted the trace of  $\hat{\tau}(v_i, v_j) \langle \rho \rangle$  as the squared velocity fluctuation,  $q^2 := \hat{\tau}(v_i, v_i) / \langle \rho \rangle$ . The evolution of the cor-

<sup>4</sup> For a review, see Röpke & Schmidt (2009).

responding turbulent energy,  $e_t = \frac{1}{2}q^2$ , is given by

$$\frac{\partial}{\partial t} \langle \rho \rangle e_t + \frac{\partial}{\partial r_j} \hat{v}_j \langle \rho \rangle e_t = \mathbb{D} + \Sigma + \Gamma - \langle \rho \rangle (\lambda + \epsilon), \quad (11)$$

where

$$\mathbb{D} = -\frac{\partial}{\partial r_j} \left[ \frac{1}{2} \hat{\tau} (v_j, v_i, v_i) - \mu + \kappa \right] \quad (12)$$

$$\Sigma = -\hat{\tau}_{ij} \partial v_i / \partial r_j \quad (13)$$

$$\Gamma = +\hat{\tau} (v_i, g_i) \quad (14)$$

$$\langle \rho \rangle \lambda = \left[ \langle p \rangle \frac{\partial}{\partial r_i} \hat{v}_i - \langle p \frac{\partial}{\partial r_i} v_i \rangle \right] \quad (15)$$

$$\langle \rho \rangle \epsilon = - \left[ \langle \sigma'_{ij} \rangle \frac{\partial}{\partial r_j} \hat{v}_i - \langle \sigma'_{ij} \frac{\partial}{\partial r_j} v_i \rangle \right], \quad (16)$$

and

$$-\mu = \langle v_i p \rangle - \hat{v}_i \langle p \rangle \quad (17)$$

$$-\kappa = \langle v_i \sigma'_{ij} \rangle - \hat{v}_i \langle \sigma'_{ij} \rangle. \quad (18)$$

The explicit forms of the quantities  $\mathbb{D}$ ,  $\lambda$ ,  $\epsilon$ ,  $\Gamma$  and  $\hat{\tau}(v_i, v_j)$  are unknown and have to be modeled in terms of closure relations, i. e., functions of the filtered flow quantities (or their derivatives) and the turbulent energy  $e_t$ . The closures for all these terms represent the SGS model.

## 2.2. Subgrid scale closures

In the following we consider a simplified set of equations to model the influence of the turbulent small scale (SGS) motions on the numerically resolved scales  $\ell \geq \ell_\Delta$ , neglecting the influence of the viscous stress tensor  $\langle \sigma'_{ij} \rangle$  (which is a very good approximation for high Reynolds numbers) and the turbulent transport of heat given by the divergence of  $\hat{\tau}(v_j, e_{int})$  in equations (6) and (7). Moreover, gravitational effects on unresolved scales are neglected, i. e., we set  $\Gamma = 0$  in equation (11) for the turbulent energy. For the terms (12), (13), and (16), we adopt SGS closures that have been applied in large eddy simulations of incompressible turbulence. The numerical study by Schmidt et al. (2006) demonstrated that these closures can be carried over to transonic turbulence, for which the unresolved turbulent velocity fluctuations are small compared to the speed of sound. Additionally, we utilize the pressure-dilatation model of Sarkar (1992) in order to account for moderate compressibility effects. Since we concentrate on the dynamics of the gas in the ICM, where the Mach numbers may locally approach unity, the SGS closures outlined subsequently serve as a reasonable approximation. In supersonic flow regions, on the other hand, the SGS model is deactivated in order to maintain stability (see §2.4).

The flux of kinetic energy from resolved scales toward subgrid scales, i. e., the rate of turbulent energy production, is given by the contraction of the turbulent stress tensor and the Jacobian of the resolved velocity field. Since  $\hat{\tau}_{kk} = \langle \rho \rangle q^2$ , we split the tensor in a symmetric trace-free part  $\hat{\tau}_{ij}^*$  and a diagonal part:

$$\hat{\tau}_{ij} = \hat{\tau}_{ij}^* + \frac{1}{3} \delta_{ij} \langle \rho \rangle q^2. \quad (19)$$

The model for  $\hat{\tau}_{ij}^*$  is based on the turbulent viscosity hypothesis (Boussinesq 1877), which means that  $\hat{\tau}_{ij}^*$  is assumed to be of the same form as the stress tensor  $\sigma'_{ij}$

of a Newtonian fluid. Hence,

$$\hat{\tau}_{ij}^* = -2\eta_t S_{ij}^* \quad (20)$$

with a turbulent dynamic viscosity  $\eta_t = \langle \rho \rangle \nu_t = \langle \rho \rangle C_\nu l_\Delta q$  and

$$S_{ij}^* = \frac{1}{2} \left( \frac{\partial}{\partial r_j} \hat{v}_i + \frac{\partial}{\partial r_i} \hat{v}_j \right) - \frac{1}{3} \delta_{ij} \frac{\partial}{\partial r_k} \hat{v}_k. \quad (21)$$

The turbulence production term is therefore modeled as

$$\hat{\tau}(v_i, v_j) = -2\langle \rho \rangle C_\nu l_\Delta q S_{ij}^* + \frac{1}{3} \delta_{ij} \langle \rho \rangle q^2. \quad (22)$$

We set  $C_\nu = 0.05$  (Sagaut 2006).

The SGS transport of turbulent energy (equation 12) is modeled by a gradient-diffusion hypothesis, stating that the non-linear term is proportional to the turbulent velocity  $q^2$  gradient (Sagaut 2006)

$$\mathbb{D} = \frac{\partial}{\partial r_i} C_\mathbb{D} \langle \rho \rangle l_\Delta q^2 \frac{\partial}{\partial r_i} q. \quad (23)$$

The diffusion coefficient has been calibrated to  $C_\mathbb{D} \approx 0.4$  by numerical experiments (Schmidt et al. 2006).

For sufficiently high Reynolds numbers, viscous energy dissipation (equation 16) becomes entirely an SGS effect. The most simple expression that can be built from the characteristic turbulent velocity and length scale for dissipation is

$$\epsilon = C_\epsilon \frac{q^3}{l_\Delta}. \quad (24)$$

For our simulations we set  $C_\epsilon = 0.5$  (Sagaut 2006).

The effect of unresolved pressure fluctuations in compressible turbulence is described by the  $\lambda$  term (equation 15). A simple closure for subsonic turbulent flow is (Deardorff 1973)

$$\lambda = C_\lambda q^2 \frac{\partial}{\partial r_i} \hat{v}_i, \quad (25)$$

where  $C_\lambda = -\frac{1}{5}$  (Fureby et al. 1997). Sarkar (1992) performed simulations of simple compressible flows and investigated the influence of the mean Mach number of the flow on the turbulent dissipation  $\epsilon$  and the pressure dilatation  $\lambda$ . Based on this analysis he suggested different models for these terms, which we will describe in the following sections. These modifications have been proven to yield good results for transonic turbulence (Shyy & Krishnamurthy 1997).

As a major effect of compressibility from direct numerical simulation, Sarkar (1992) identified that the growth rate of kinetic energy decreases if the initial turbulent Mach number increases. This means that the dissipation of kinetic energy (and, therefore, of the turbulent energy) increases with the turbulent Mach number  $M_t = q/c_s$ , where  $c_s$  is the speed of sound. Sarkar (1992) suggested to account for this effect by using

$$\epsilon = C_\epsilon \frac{q^3}{l_\Delta} (1 + \alpha_1 M_t^2) \quad (26)$$

with  $\alpha_1 = 0.5$  as a model for the dissipation of turbulent energy.

Based on a decomposition of all variables of the equa-

tion for instantaneous pressure

$$\frac{\partial^2}{\partial r_i^2} p = \frac{\partial^2}{\partial t^2} \rho - \frac{\partial^2}{\partial r_i \partial r_j} (\rho v_i v_j - \sigma'_{ij}) \quad (27)$$

into a mean and a fluctuating part and comparisons with direct numerical simulations of simple compressible flows Sarkar (1992) proposed a different model for the pressure dilatation

$$\lambda = \alpha_2 M_t \hat{\tau}_{ij}^* \frac{\partial \hat{v}_i}{\partial r_j} - \alpha_3 M_t^2 C_\epsilon \frac{q^3}{l_\Delta} - 8\alpha_4 M_t^2 p_t \frac{\partial \hat{v}_k}{\partial r_k} \quad (28)$$

with  $\alpha_2 = 0.15, \alpha_3 = 0.2$  obtained from a curve fit of the model with direct numerical simulation (DNS). Unfortunately, Sarkar (1992) does not specify a value for  $\alpha_4$ , so there is some confusion in the literature about it. For example, Shyy & Krishnamurty (1997) set  $\alpha_4 = 0$  and still found the Sarkar model in good agreement with their DNS simulation. In this work, we adopt  $\alpha_4 = \alpha_2^2/2$ . With this choice, the effective production of turbulent energy vanishes for a turbulent Mach number  $M_t = 1/\alpha_2$ . In the following we will sometimes refer to the ‘‘Sarkar SGS’’ when the equations (26) and (28) are used in the model.

### 2.3. Filtered equations in comoving coordinates

Simulations with a comoving cosmological background require a formulation of the filtered fluid dynamical equations in comoving coordinates. Applying the Germano decomposition (§2.1) in a comoving coordinate system with spatially homogeneous scale factor  $a(t)$ , we obtain<sup>5</sup>

$$\begin{aligned} \frac{\partial}{\partial t} \langle \bar{\rho} \rangle + \frac{1}{a} \frac{\partial}{\partial x_j} \hat{u}_j \langle \bar{\rho} \rangle &= 0, \quad (29) \\ \frac{\partial}{\partial t} \langle \bar{\rho} \rangle \hat{u}_i + \frac{1}{a} \frac{\partial}{\partial x_j} \hat{u}_j \langle \bar{\rho} \rangle \hat{u}_i &= -\frac{1}{a} \frac{\partial}{\partial x_i} \langle \bar{p} \rangle + \langle \bar{\rho} \rangle \hat{g}_i^* \\ &\quad - \frac{1}{a} \frac{\partial}{\partial x_j} \hat{\tau}(u_i, u_j) - \frac{\dot{a}}{a} \langle \bar{\rho} \rangle \hat{u}_i, \quad (30) \\ \frac{\partial}{\partial t} \langle \bar{\rho} \rangle e_{\text{res}} + \frac{1}{a} \frac{\partial}{\partial x_j} \hat{u}_j \langle \bar{\rho} \rangle e_{\text{res}} &= -\frac{1}{a} \frac{\partial}{\partial x_i} \hat{u}_i \langle \bar{p} \rangle - \frac{1}{a} \langle \bar{\rho} \rangle \hat{u}_i \hat{g}_i^* \\ &\quad - \frac{\dot{a}}{a} (\langle \bar{\rho} \rangle e_{\text{res}} + \frac{1}{3} \langle \bar{\rho} \rangle \hat{u}_i \hat{u}_i + \langle \bar{p} \rangle) \\ &\quad + \langle \bar{\rho} \rangle (\lambda + \epsilon) - \frac{1}{a} \hat{u}_i \frac{\partial}{\partial x_j} \hat{\tau}(u_i, u_j) \quad (31) \\ \frac{\partial}{\partial t} \langle \bar{\rho} \rangle e_t + \frac{1}{a} \frac{\partial}{\partial x_j} \hat{u}_j \langle \bar{\rho} \rangle e_t &= \mathbb{D} + \Gamma - \langle \bar{\rho} \rangle (\lambda + \epsilon) \\ &\quad - \frac{1}{a} \hat{\tau}(u_j, u_i) \frac{\partial}{\partial x_j} \hat{u}_i - 2 \frac{\dot{a}}{a} \langle \bar{\rho} \rangle e_t. \quad (32) \end{aligned}$$

With respect to the non-comoving equations listed in §2.1, the only term to implement additionally is the last one on the right-hand side of equation (32). Furthermore, SGS closures have to be expressed in terms of the Jacobian of the velocity in comoving coordinates,

$$J_{ij} = \frac{\partial}{\partial r_i} v_j = \frac{1}{a} \frac{\partial}{\partial x_i} u_j + \frac{\dot{a}}{a} \delta_{ij}. \quad (33)$$

In particular, the trace-free rate of strain tensor in co-

<sup>5</sup> The comoving density  $\bar{\rho} = a^3 \rho$  and the comoving pressure  $\bar{p} = a^3 p$  are introduced to shorten the equations.

moving coordinates is given by

$$S_{ij}^* = \frac{1}{2} (J_{ij} + J_{ji}) - \frac{1}{3} \delta_{ij} J_{kk}. \quad (34)$$

### 2.4. Limits of the SGS model

Numerical difficulties result from constraints on the validity of SGS closures. In particular, the turbulent viscosity hypothesis expressed by equation (22) was devised to account for the production of turbulence by shear in moderately compressible flow. This is typically encountered in the dense, central regions of galaxy clusters. However, the surrounding low-density gas can be accelerated very quickly in the gravitational field of the cluster. Moreover, high velocity gradients are encountered in the vicinity of shocks which are produced by gas accretion onto filaments, sheets, and halos as well as by the merging of substructures. In order to inhibit unphysical production of turbulent energy by these mechanisms, which are not accommodated in the present formulation of the SGS model, several numerical safeguarding mechanisms have been introduced.

First of all, we implemented a simple shock detector which identifies strong negative divergence. A cell is marked if the velocity jump corresponding to the negative divergence becomes greater than the sound speed across the cell width  $l_\Delta$ :

$$-\frac{\partial v_i}{\partial r_i} > \frac{c_s}{l_\Delta}. \quad (35)$$

In cells satisfying the above criterion, the source and transport terms of the SGS model (equations 22 and 23) are disabled. The turbulent energy is only advected in these cells, and no coupling to the the velocity and the resolved energy is applied.

Besides the previous check, an additional constraint is imposed on the magnitude of the turbulent energy, via the turbulent Mach number. Basically, the SGS model breaks down once  $M_t$  becomes large compared to unity, therefore a threshold for this quantity is set to  $M_{t,\text{max}} = \sqrt{2}$ . This value for the maximal turbulent Mach number is motivated by the theory of isothermal turbulence, where the effective gas pressure can be expressed as

$$p_{\text{eff}} = \rho c_s^2 + \frac{1}{3} \rho q^2 = \gamma_{\text{eff}} \rho c_s^2, \quad (36)$$

and, consequently,  $p_{\text{eff}}$  is limited to the adiabatic value  $\frac{5}{3} \rho c_s^2$ . We verified that this threshold does not harm our cluster simulations, because in the hotter gas phases ( $T > 10^5$  K) turbulence is largely subsonic, and the threshold is rarely reached.

A supplementary low temperature cutoff ensures that the sound speed does not drop to excessively low values, which occur in cosmological simulations especially in the low-density voids. We set the lower limit of the temperature to  $T_{\text{min}} = 10$  K. This threshold ensures numerical stability and does not affect the baryon physics appreciably, apart from possibly making the shocks on accreting structures weaker.

### 2.5. Combining AMR and LES

In Large Eddy Simulations (LES), the filtered equations (29-32) are solved using an SGS model as outlined in the previous Section. However, the closure rela-

tions we use and, in fact, the very concept of SGS turbulence energy only applies if the velocity fluctuations on subgrid scales are nearly isotropic. This limits the LES methodology to flows where all anisotropies stemming from large scale features, like boundary conditions or external forces, can be resolved. In the FEARLESS method, the grid resolution  $\ell_\Delta$  is locally adjusted by adaptive mesh refinement (AMR) in order to ensure that the anisotropic, energy-containing scales are resolved everywhere. On the other hand, it is assumed that turbulence is asymptotically isotropic on length scales comparable to or less than  $\ell_\Delta$ . It is very difficult to justify the latter assumption *a priori*, because there are no refinement criteria that would guarantee asymptotic isotropy on the smallest resolved length scales. By careful analysis of simulation results, however, one can gain confidence that AMR resolves turbulent regions appropriately.

As an infrastructure for the implementation of FEARLESS, we chose Enzo v. 1.0 (O’Shea et al. 2005), an AMR, grid-based hybrid (hydrodynamics plus N-Body) code based on the PPM solver (Colella & Woodward 1984) and especially designed for simulations of cosmological structure formation. When a grid location is flagged for refinement in Enzo, a new finer grid is created, and the cell values on the finer grid are generated by interpolating them from the coarser grid using a conservative interpolation scheme. At each timestep of the coarse grid, the values from the fine grid are averaged and the values computed on the coarse grid (in the region where fine and coarse grid overlap) are replaced. However, this approach does not account for the inherent scale-dependence of the turbulent energy. Assuming Kolmogorov scaling (Kolmogorov 1941; Frisch 1995), the turbulent energies at two different levels of refinement with cell size  $l_{\Delta,1}$  and  $l_{\Delta,2}$ , respectively, are statistically related by

$$\frac{e_{t,1}}{e_{t,2}} = \frac{q_1^2}{q_2^2} \sim \left( \frac{l_{\Delta,1}}{l_{\Delta,2}} \right)^{2/3}. \quad (37)$$

Using this scaling relation, we implemented a simple algorithm to adjust the turbulent energy budget when grids are refined or derefined. The following procedure is used once a grid is refined:

1. Interpolate the values from the coarse to the fine grid using the standard interpolation scheme from Enzo.
2. On the finer grid, correct the values of the velocity components,  $\hat{v}_i$ , and the turbulent energy,  $e_t = \frac{1}{2}q^2$ , as follows

$$\hat{v}'_i = \hat{v}_i \sqrt{1 + \frac{e_t}{\hat{e}_{\text{kin}}} (1 - r_\Delta^{-2/3})}, \quad (38)$$

$$e'_t = e_t r_\Delta^{-2/3}, \quad (39)$$

where  $\hat{e}_{\text{kin}}$  is the resolved kinetic energy,  $r_\Delta$  is the refinement factor of the mesh, and the primed quantities are the final values on the fine grid. The resolved energy is adjusted such that the sum of resolved energy and turbulent energy remains conserved.

Apart from adjusting the energy budget, the resolved flow should feature velocity fluctuations on length scales smaller than the cutoff length of the parent grid if a

refined grid is generated. To address this problem we observe that the smallest pre-existing eddies that are inherited from the parent grid will produce new eddies of smaller size within a turn-over time. Although this implies a small delay because of the higher time resolution of the refined grid, the flow will rapidly adjust itself to the new grid resolution.

For grid derefinement we reverse this procedure:

1. Average the values from the fine grid and replace the corresponding values on the coarse grid
2. In the regions of the coarse grid covered by finer grids, correct the velocity components and the turbulent energy:

$$e'_t = e_t r_\Delta^{2/3}, \quad (40)$$

$$\hat{v}'_i = \hat{v}_i \sqrt{1 - \frac{e_t}{\hat{e}_{\text{kin}}} (r_\Delta^{2/3} - 1)}. \quad (41)$$

Here, primed quantities denote the final values on the coarse grid. The resolved energy is adjusted to maintain energy conservation and a positive kinetic energy.

### 3. NUMERICAL TESTS

We applied two consistency tests of the SGS model in simulations of forced isotropic turbulence in a periodic box. First, energy conservation was checked in adiabatic turbulence simulations and, second, the scaling of the turbulent energy over several levels of resolution was investigated for isothermal turbulence. To simulate driven turbulent flow, a random forcing mechanism based on the Ornstein-Uhlenbeck process was applied (Schmidt 2004). This process generates a solenoidal (i. e., divergence-free) stochastic force field which accelerates the fluid at large length scales  $l \approx l_0$ , where  $l_0$  is the size of the computational box. The strength of the force field is characterized by a forcing Mach number  $M_f$ . The Mach numbers of the flow becomes comparable to  $M_f$  once the forcing has been applied over a period of time that is defined by the integral time  $t_{\text{int}} = l_0/M_f c_s$ .

#### 3.1. Energy conservation

For global energy conservation it turned out to be important to compute the turbulent stress term in equation (6) indirectly as

$$\hat{v}_i \frac{\partial}{\partial r_j} \hat{\tau}(v_i, v_j) = \frac{\partial}{\partial r_j} \hat{v}_i \hat{\tau}(v_i, v_j) - \hat{\tau}(v_j, v_i) \frac{\partial}{\partial r_j} \hat{v}_i, \quad (42)$$

The reason behind it is that only by using this rearrangement of the terms we can ensure that we do not introduce small numerical errors which would violate the local sum

$$\frac{\partial}{\partial r_j} \hat{v}_i \hat{\tau}(v_i, v_j) = \hat{v}_i \frac{\partial}{\partial r_j} \hat{\tau}(v_i, v_j) + \hat{\tau}(v_j, v_i) \frac{\partial}{\partial r_j} \hat{v}_i. \quad (43)$$

leading to a big error in global energy conservation.

As a testing case, we run a LES of driven turbulence as outlined above on a static grid of  $256^3$  grid points and periodic boundary conditions. The adiabatic index  $\gamma = \frac{5}{3}$  and  $M_f = 0.68$ .

Figure 1 shows the typical time development of the mass-weighted mean energies in our simulation including the energy  $e_f$  injected into the system by random forcing. It is evident from the curve of the turbulent energy that

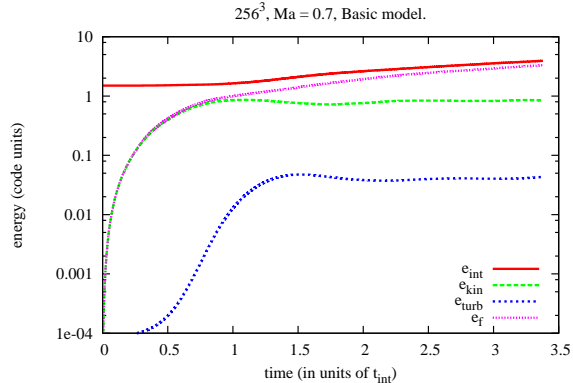


FIG. 1.— Time evolution of mass-weighted energy averages in the driven turbulence simulation. The different energy components are indicated by colors.

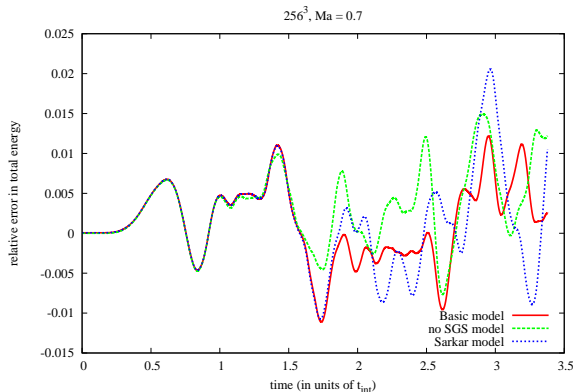


FIG. 2.— Relative error of the total energy in the driven turbulence simulation. The different lines indicate simulations run with different versions of the SGS model, or without it, as shown in the legend.

after one integral time scale, our simulation reaches an equilibrium between production and dissipation of turbulent energy.

In Fig. 2, we plot the time development of the relative error  $\frac{\Delta e(t)}{e(0)}$  of the mean total energy, defined as the sum of the mass-weighted means of internal energy, kinetic energy, turbulent energy minus the injected energy by the forcing,

$$\hat{e}_{\text{tot}} = \hat{e}_{\text{int}} + \hat{e}_{\text{kin}} + e_t - \hat{e}_f, \quad (44)$$

where  $\hat{e} = \frac{\langle \rho e \rangle}{\langle \rho \rangle}$ . It demonstrates that with our basic model, the relative error in energy is comparable to the error without SGS model, and is around 1%. The energy conservation of the model using the Sarkar modifications is equally good.

It is also instructive to plot the difference between the energy contributions (internal and kinetic energy) in the simulations with and without the SGS model. These differences are shown in Fig. 3. One can conclude from this figure that, at the beginning of the turbulent driving, the turbulent energy produced in our simulation with SGS model is found in the kinetic energy of the simulation without SGS model. In contrast, from  $t = 1.2 t_{\text{int}}$  on, most of the turbulent energy can be found in the internal energy of the simulation without SGS model. Turbulent energy can therefore be interpreted as a kind of buffer

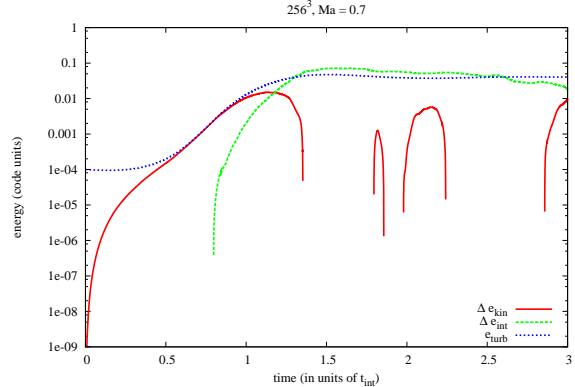


FIG. 3.— Time evolution of the energy differences (red line: kinetic energy; green line: internal energy) between simulations with and without the SGS model (basic version), compared to the evolution of the turbulent energy (blue line).

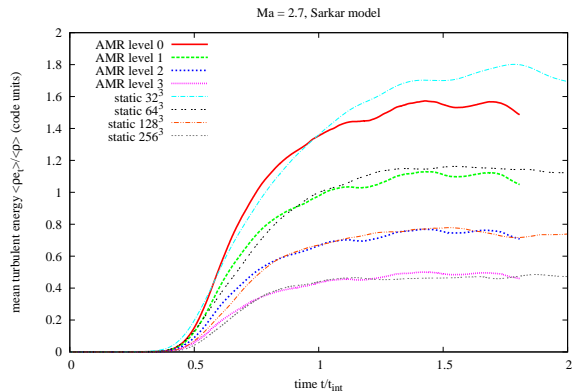


FIG. 4.— Thick lines: mean mass-weighted turbulent energy for each level of the AMR simulation, using our procedure of transferring turbulent energy at grid refinement/derefinement. Thin lines: the corresponding evolution of turbulent energy of the static grid simulations. The colors indicate the AMR level or the static grid resolution.

which prevents the kinetic energy in our simulation to be converted instantly into thermal energy.

### 3.2. Scaling of turbulent energy

A necessary condition for the validity of the turbulent energy transfer algorithms explained in §2.5 is that an AMR simulation should approximately reproduce the results of static grid simulations corresponding to the different levels of refinement. To test this, we compared an AMR simulation of driven turbulence with a  $32^3$  root grid resolution and three additional levels (with a refinement factor of 2 between each level) to three static grid simulations with resolutions of  $32^3$ ,  $64^3$ ,  $128^3$  and  $256^3$ . In order to allow for the comparison of averaged quantities, refinement of the entire domain was enforced at all levels of the AMR simulation. In order to reach a statistically stationary root-mean-square (rms) Mach number, we ran the simulations for nearly isothermal gas with  $\gamma = 1.01$  (for adiabatic turbulence, after an initial rise, the rms Mach number gradually decreases with time because of the dissipative heating of the gas). We used a supersonic forcing Mach number,  $M_f = 2.7$ , to check whether a consistent turbulent energy budget could be achieved for highly compressible turbulence, albeit the scaling relations (37) of incompressible turbulence were

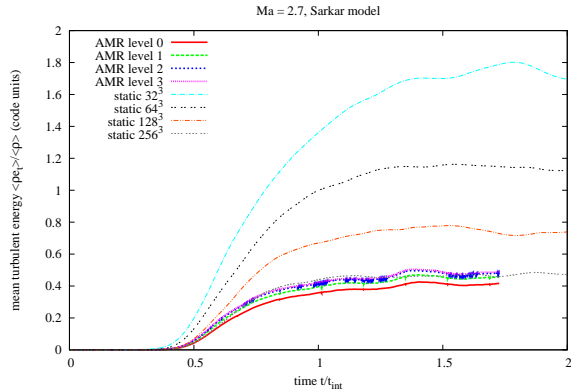


FIG. 5.— Thick lines: mean mass-weighted turbulent energy for each level of the AMR simulation without transferring turbulent energy at grid refinement/derefinement. Thin lines: the corresponding evolution of turbulent energy of the static grid simulations. The colors indicate the AMR level or the static grid resolution.

utilized.

The results of this consistency check can be seen in Fig. 4. We observe that the time development of the mean turbulent energy is very similar on the different levels of the AMR simulation compared to the static grid simulations, except for some deviations at the root level. On the other hand, comparing these results to a simulation without correcting turbulent energy at grid refinement/derefinement (Fig. 5), it is evident that the scaling of the turbulent energy in the latter case is inconsistent.

#### 4. DETAILS OF THE CLUSTER SIMULATIONS

##### 4.1. Simulation setup

We performed simulations of cluster formation with Enzo, following Iapichino & Niemeyer (2008). We will compare two runs: one of them was done with the public version of Enzo (without SGS model), and the other with FEARLESS implemented, in its version including the Sarkar correction (equations 26 and 28). The simulations were done using a flat  $\Lambda$ CDM background cosmology with a dark energy density  $\Omega_\Lambda = 0.7$ , a total (including baryonic and dark matter) matter density  $\Omega_m = 0.3$ , a baryonic matter density  $\Omega_b = 0.04$ , the Hubble parameter set to  $h = 0.7$ , the mass fluctuation amplitude  $\sigma_8 = 0.9$ , and the scalar spectral index  $n = 1$ . Both simulations were started with the same initial conditions at redshift  $z_{\text{ini}} = 60$ , using the Eisenstein & Hu (1999) transfer function, and evolved to  $z = 0$ . The simulations are adiabatic with a heat capacity ratio  $\gamma = 5/3$  assuming a fully ionized gas with a mean molecular weight  $m_\mu = 0.6$  u. Cooling physics, magnetic fields, feedback, and transport processes are neglected.

The simulation box has a comoving size of  $128 \text{ Mpc h}^{-1}$ . It is resolved with a root grid (level  $l = 0$ ) of  $128^3$  cells and  $128^3$  N-body particles. A static child grid ( $l = 1$ ) is nested inside the root grid with a size of  $64 \text{ Mpc h}^{-1}$ ,  $128^3$  cells and  $128^3$  N-body particles. The mass of each particle in this grid is  $9 \times 10^9 M_\odot \text{ h}^{-1}$ . Inside this grid, in a volume of  $38.4 \text{ Mpc h}^{-1}$ , adaptive grid refinement from level  $l = 2$  to  $l = 7$  is enabled using an overdensity refinement criterion as described in Iapichino & Niemeyer (2008) with an overdensity factor  $f = 4.0$ . The refinement factor between two levels was set to  $r_\Delta = 2$ , allowing for an effective resolution of

$7.8 \text{ kpc h}^{-1}$ .

The static and dynamically refined grids were nested around the place of formation of a galaxy cluster, identified using the HOP algorithm (Eisenstein & Hut 1998). Since the realization of the initial conditions was chosen identical to Iapichino & Niemeyer (2008), this study is based on the same cluster analyzed in that work. The cluster has a virial mass of  $M_{\text{vir}} = 5.95 \times 10^{14} M_\odot \text{ h}^{-1}$  and a virial radius of  $R_{\text{vir}} = 1.37 \text{ Mpc h}^{-1}$ .

##### 4.2. Local Kolmogorov scaling

In static grid simulations one often chooses to use the grid resolution  $l_\Delta$  as characteristic length scale to compute a characteristic velocity or eddy turnover time for this scale. However, in an AMR code it is not trivial to compute the turbulent velocity  $q_l$  associated with a characteristic length scale  $l = l_\Delta$ , since  $l_\Delta$  varies in time and space. To circumvent this difficulty, we assume that below the grid resolution turbulent velocity locally scales according to Kolmogorov

$$q(l) \sim l^{1/3}. \quad (45)$$

We thereby assume that locally a Kolmogorov-like energy cascade sets in, at a length scale given by the resolution of the grid at that position. This local hypothesis holds here only for the analysis of our simulations, and is similar to the assumption done in §2.5 for managing the grid refinement and derefinemnt.

As a characteristic scale of our analysis, we choose the length scale of our highest resolved regions, which is  $l_{\text{min}} = 7.8 \text{ kpc h}^{-1}$ . The turbulent velocity in the most finely resolved regions can be computed directly from the values of the turbulent energy  $q(l) = \sqrt{2e_t}$  on the grid; the turbulent velocity in less finely refined regions is scaled down according to our local Kolmogorov hypothesis as

$$q(l_{\text{min}}) = q(l_\Delta) \left( \frac{l_{\text{min}}}{l_\Delta} \right)^{2/3}. \quad (46)$$

#### 5. RESULTS

##### 5.1. Turbulent energy scaling in the cluster simulation

In §3.2, we studied the temporal evolution of the turbulent energy at different resolutions in a simulation of driven turbulence. In this section, we repeat this analysis for our FEARLESS cluster simulation. Figure 6 shows the evolution of the mass-weighted mean turbulent energy for every level of our AMR simulation. We see from the plot that the turbulent energy on the higher AMR levels  $l$  (meaning at smaller scales) is higher at early times ( $2 \text{ Gyr} < t < 6 \text{ Gyr}$ ). Later this picture changes, but not completely. For example, the turbulent energy at  $l = 4$  stays above the turbulent energy at  $l = 3$  throughout the simulation. The magnitude of  $e_t$  along the AMR levels suggests to locate the turbulence injection length scale between 125 and 250  $\text{kpc h}^{-1}$ , corresponding to the effective resolutions of levels 3 and 4. This is only a rough qualitative estimate, but nevertheless in agreement with theoretical expectations (e.g. Subramanian et al. 2006).

Particularly noteworthy are the turbulent energy fluctuations on smaller scales at the time  $2 \text{ Gyr} < t < 6 \text{ Gyr}$ , corresponding to a redshift  $z = 3 - 1$ . We can interpret these large fluctuations as evidence for violent major mergers that happen at that time, producing turbulent energy which is then dissipated into internal energy,

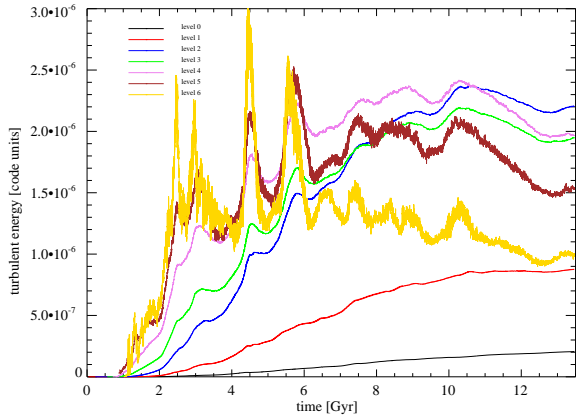


FIG. 6.— Time evolution of the mean turbulent energy for each level of refinement. This analysis has been performed on a test run identical to that described in §4.1 with only six AMR levels.

heating up the cluster gas. However, at  $t > 12$  Gyr the simulation seems to globally reach some kind of stable state, comparable to what has been found in the driven turbulence simulations.

### 5.2. Spatial distribution of turbulent energy

Before performing a quantitative analysis of the cluster properties in the FEARLESS run, it is useful to visually inspect the generation and the spatial distribution of the turbulent energy in the ICM and around the cluster, in order to compare the simulations with the theoretical expectations of cluster mergers. Figs. 7 and 8 present a time series of density and turbulent velocity slices, where several merger events in the cluster outskirts can be identified.

In the density slice at redshift  $z = 0.15$  (Fig. 7a), we can see a filament extending from the lower left to the upper right corner of the figure; material is falling onto the cluster along this structure. On both sides, the inflow of relatively cold gas from the filament onto the ICM produces a moderate increase of turbulent energy (cf. Nagai & Kravtsov 2003). From the upper right side there is not only a smooth inflow of matter, but two small clumps are approaching the cluster. During the simulation these two clumps merge with the main cluster (Figs. 7c to 8c) and one of them (on the left) is assimilated completely at redshift  $z = 0$ . A substructure approaches the cluster from the lower left corner along the filament (Fig. 8a) and another one is visible only at  $z = 0.05$  just to the right of the cluster core, when it crosses the slicing plane.

The merging process can be followed much more easily in terms of production of turbulent energy, visualized by the turbulent velocity  $q = \sqrt{2e_t}$ . In Fig. 7b at  $z = 0.15$ , a marked peak of turbulent energy in the center of our cluster, resulting from a former massive merger, can be seen. The turbulent energy produced by this merger declines (Figs. 7d to 8d) and at  $z = 0$  it is dissipated into internal energy nearly completely, as confirmed by our further analysis in §5.4.

The two approaching clumps described above continue to drive turbulence in the cluster. Thereby, the left clump can be identified in the turbulent velocity slice at  $z = 0.15$  (Fig. 7b) as a ring-like structure, showing that turbulence is not produced at the center of the infalling

TABLE 1  
ENERGY CONTRIBUTIONS IN A SPHERE OF  $r = R_{\text{vir}}$ ,  
CENTERED AT THE CLUSTER CORE, AT  $z = 0$ .

Quantity	Adiabatic run	FEARLESS run
$E_{\text{tot}}$ [ $10^{63}$ erg]	2.6458	2.6426 (-0.1%)
$E_{\text{int}}$ [ $10^{63}$ erg]	2.1982	2.2082 (+0.5%)
$E_{\text{kin}}$ [ $10^{62}$ erg]	4.476	4.168 (-6.9%)
$E_t$ [ $10^{61}$ erg]	...	1.762

NOTE. — The total energy  $E_{\text{tot}}$  is defined as the sum of  $E_{\text{int}}$ ,  $E_{\text{kin}}$  and, in the FEARLESS run,  $E_t$ . The turbulent energy reported here is not scaled as described in §5.1.

clump but at the front (behind a bow shock) and in the wake of the infalling material. The right clump only shows some turbulence production in its wake, which might be due to its smaller size and smaller velocity. On their way towards the main cluster and through its ICM, both clumps show a relevant production of turbulent energy (Figs. 7d to 8b). The considerable amount of turbulent energy can even be identified after the two clumps have merged with the main cluster (Fig. 8d) and the left one is not easily visible in the corresponding density slice (Fig. 8c). From this point of view, the distribution of turbulent energy traces the local merging history of a galaxy cluster until it is dissipated into internal energy completely.

The morphological evolution of the cluster gives a clear sense of the markedly local behavior of the production and dissipation of turbulence, which is confirmed to be an intermittent process in the ICM.

### 5.3. Cluster energy budget

It is extremely difficult to apply an energy analysis similar to that performed in §3.1 to a galaxy cluster. Different than a periodic box, a galaxy cluster is an open system, with a growth over time of negative gravitational potential energy. Nevertheless, a comparison of the energy contributions of the two simulations at  $z = 0$  is useful to understand the role of the SGS model.

The results are summarized in Table 1, where the energies in a sphere centered at the cluster center and with  $r = R_{\text{vir}}$  are reported. Different than elsewhere in this work, in Table 1 the energies are not specific, i.e.  $E_{\text{tot}} = \rho e_{\text{tot}}$  etc. This choice allows a better evaluation of the energy budget but it does not differ appreciably from the analysis of specific energies, since the baryon masses in the two runs agree within 1%.

The total energy remains basically unaltered in the two simulations, whereas the most important change is the decrease of  $E_{\text{kin}}$  in the FEARLESS run. The missing kinetic energy is transferred mostly to  $E_t$ , which acts as a buffer between the resolved kinetic energy and  $E_{\text{int}}$ . The SGS model transfers energy from  $E_t$  to  $E_{\text{int}}$  either adiabatically (via the pressure dilatation term, equation 15) or irreversibly (via the dissipative term, equation 16). Turbulent dissipation is thus added to the dominant numerical dissipation, resulting in a moderate increase of  $E_{\text{int}}$ , though it is less relevant than the variation of  $E_{\text{kin}}$ .

In both runs, the kinetic energy contribution in the cluster  $E_{\text{kin}}$  is smaller than  $E_{\text{int}}$ . The mass-weighted



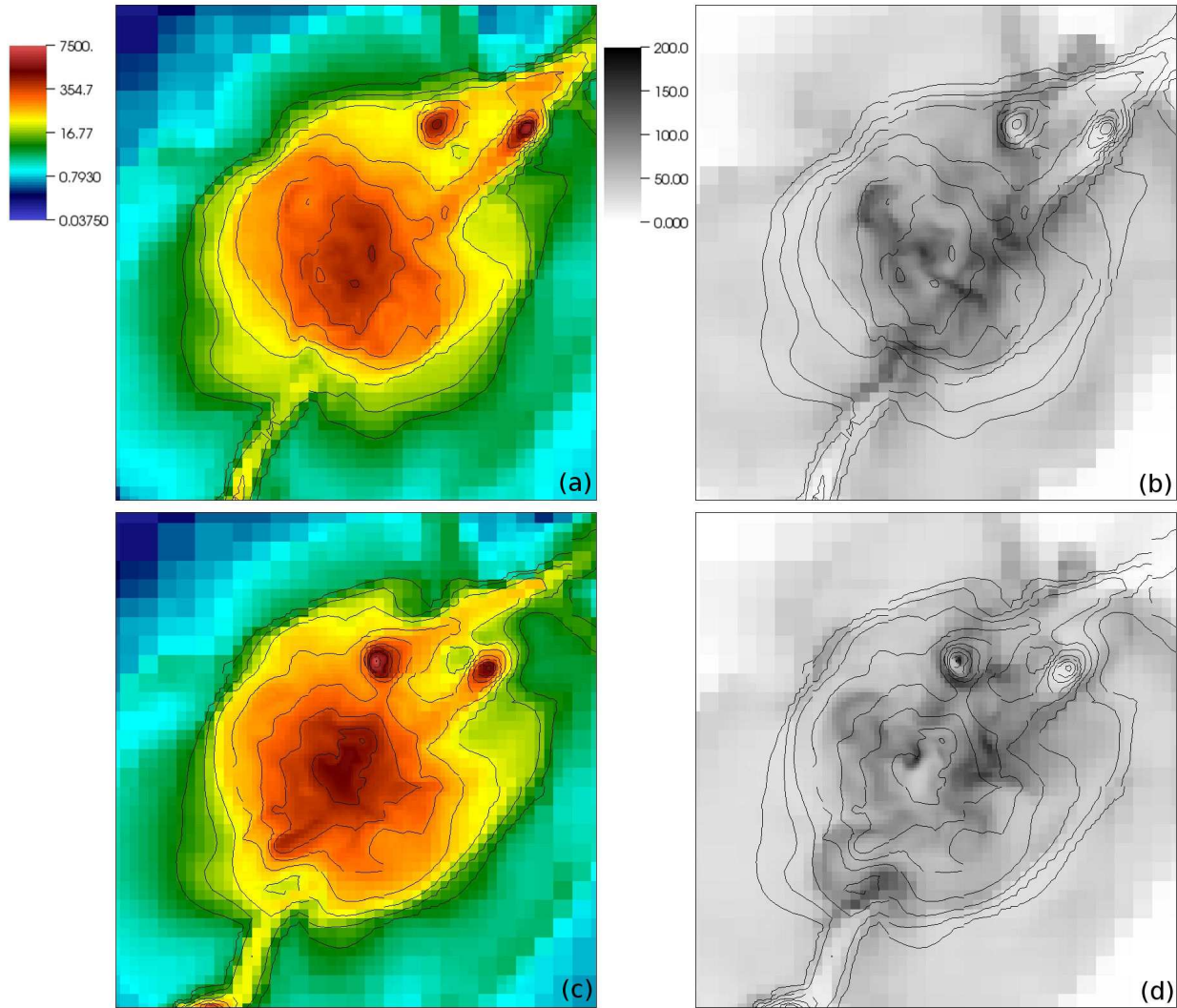


FIG. 7.— Slices of baryon density (left-hand panels, *a* and *c*) and turbulent velocity  $q = \sqrt{2e_t}$  scaled to  $7.8 \text{ kpc h}^{-1}$  (right-hand panels, *b* and *d*) at different redshifts  $z$ , for the FEARLESS run. The density is logarithmically color coded as overdensity with respect to the average baryon density in the colorbar on the left of panel *a*, whereas  $q$  is linearly coded in  $\text{km s}^{-1}$ , according to the colorbar on the left of panel *b*. The overlaid contours show density. The slices show a region of  $6.4 \times 6.4 \text{ Mpc h}^{-1}$  around the center of the main cluster followed in the simulation. Panels *a* and *b* refer to  $z = 0.15$ , panels *c* and *d* to  $z = 0.1$ .

average of the Mach number in the cluster is about 0.6, in agreement with the known fact that the flow in the ICM is, on average, mildly subsonic. In this regime it is not surprising that the subgrid energy  $E_t$  is about two orders of magnitude smaller than  $E_{\text{int}}$  on the global level. The energy contribution from unresolved scales is globally negligible, though locally turbulence can play a more significant role, as will be discussed in §5.4.

Finally, we note that the ratio of the turbulent production term  $\Sigma$  (equation 13) to the turbulent dissipation term  $\epsilon$  (equation 16) in the cluster core is

$$\frac{\Sigma}{\epsilon} = 0.93 \quad (47)$$

suggesting that the turbulent flow in the ICM is globally in a regime of near equilibrium of production and dissipation of turbulent energy.

#### 5.4. Radial profiles and local analyses

The results of §5.3, referring to global features of the galaxy cluster, will be complemented by a local comparison in terms of radial profiles of selected physical quan-

TABLE 2  
MASS-WEIGHTED AVERAGES IN A SPHERE OF  $r = 0.07 R_{\text{vir}}$ ,  
CENTERED AT THE CLUSTER CORE, AT  $z = 0$ .

Quantity	Adiabatic run	FEARLESS run
$\Sigma/\epsilon$	...	0.59
$e_{\text{tot}} [10^{16} \text{ cm}^2 \text{ s}^{-2}]$	1.3781	1.4189
$e_{\text{int}} [10^{16} \text{ cm}^2 \text{ s}^{-2}]$	1.2529	1.3030
$e_{\text{kin}} [10^{15} \text{ cm}^2 \text{ s}^{-2}]$	1.252	1.138
$e_t [10^{13} \text{ cm}^2 \text{ s}^{-2}]$	...	2.078
$p_{\text{res}}/(p_{\text{res}} + p_{\text{therm}}) [\%]$	1.46	1.52
$v_{\text{rms}} [\text{km s}^{-1}]$	196	204

ties and an analysis of the cluster core in this section.

As a first interesting result of the comparison between radial profiles in the FEARLESS simulation and in the standard adiabatic run, one can notice (Fig. 9) that the temperature profile of the FEARLESS run deviates slightly from that of the adiabatic run. This is especially apparent at the center, where  $T$  is larger in the cluster

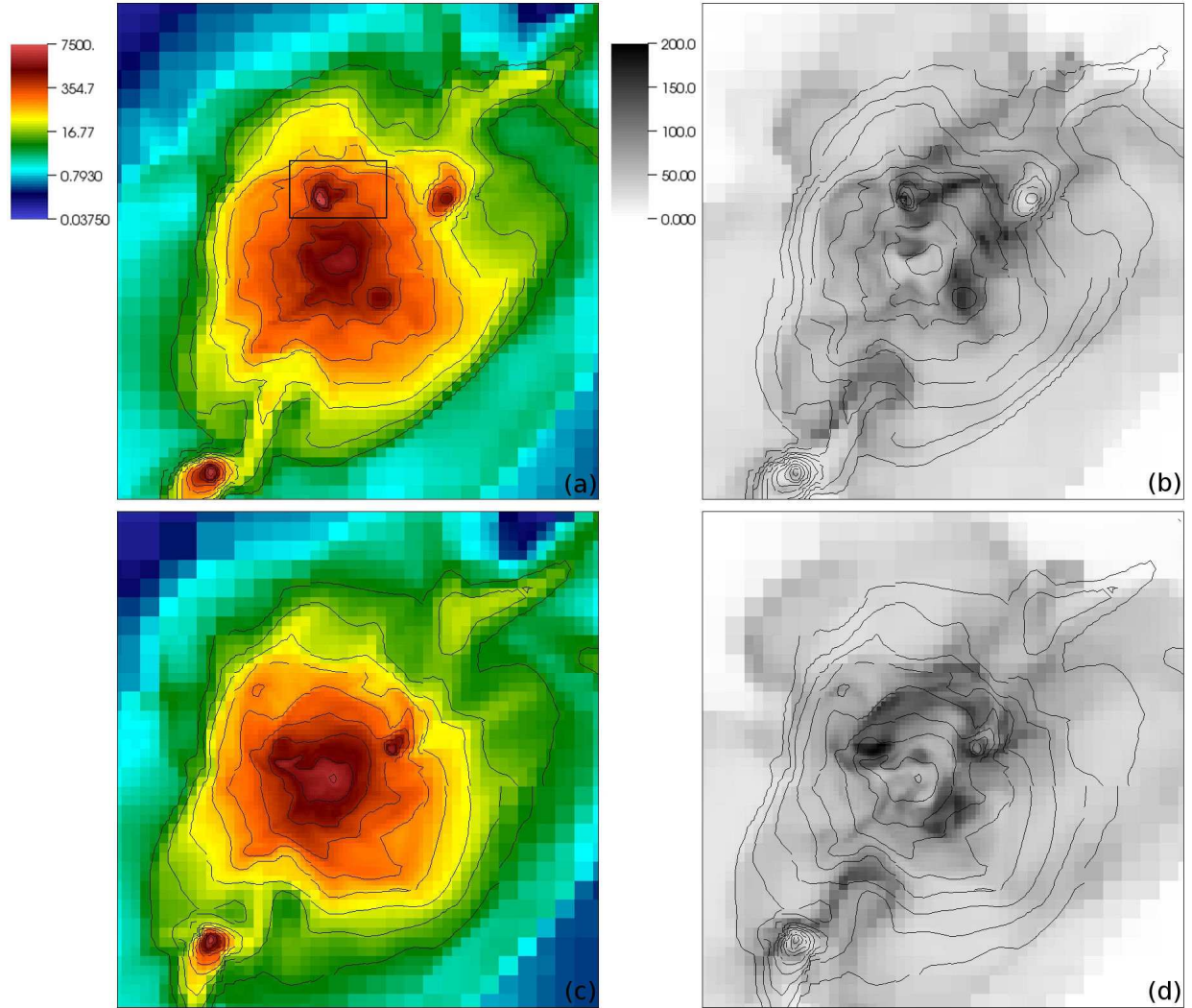


FIG. 8.— Same as Fig. 7, but in this case panels *a* and *b* refer to  $z = 0.05$ , and panels *c* and *d* to  $z = 0$ . The black rectangle in panel *a* denotes the projection on the slice of a small volume, including a subclump and its wake, analysed in Table 3.

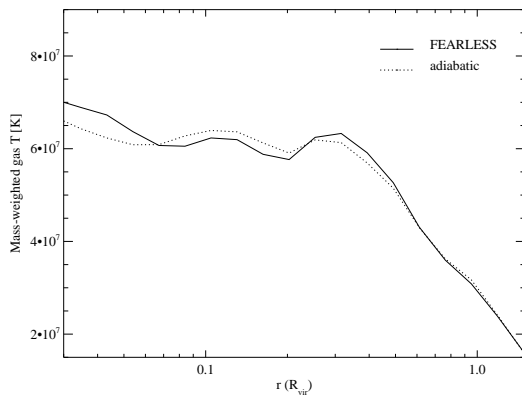


FIG. 9.— Radial profiles of mass-weighted temperature at  $z = 0$ . The dotted line refers to the simulation without SGS model, whereas the solid line is for the FEARLESS simulation (in its version including the Sarkar corrections).

core for  $r \lesssim 0.07 R_{\text{vir}}$ , with respect to the standard run. Consequently (Fig. 10) the core in the FEARLESS run is less dense, so that the ICM remains in hydrostatic equilibrium. The local energy budget in the cluster core is therefore modified by the SGS model.

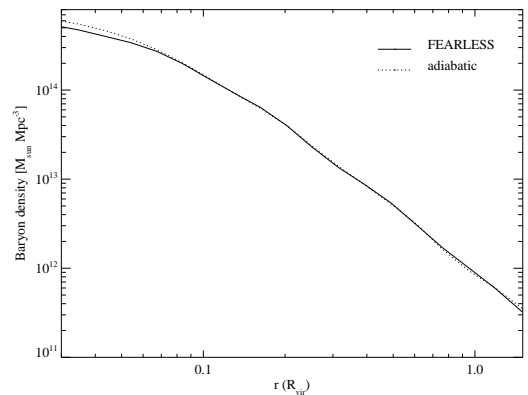


FIG. 10.— Same as Fig. 9, but showing the baryon density.

In Table 2, we explore this feature in detail, reporting the mass-weighted averages of selected variables in a sphere within  $0.07 R_{\text{vir}}$  from the cluster center. Because of the adjustment of the cluster hydrostatic equilibrium, the mass enclosed in this sphere is significantly different in the two runs (it decreases by 10 % in the FEARLESS run), thus it is more convenient to present specific ener-

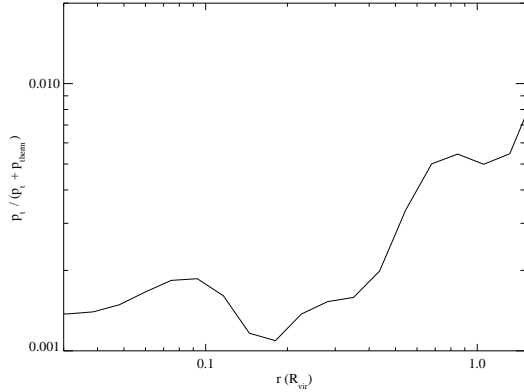


FIG. 11.— Radial profile of the turbulent contribution to the pressure support  $p_t/(p_t + p_{\text{therm}})$ , as defined in the text, for the FEARLESS simulation at  $z = 0$ .

gies in Table 2.

First, the low value of the  $\Sigma/\epsilon$  ratio indicates that, at  $z = 0$ , in the cluster core region the dissipation of turbulence is dominant with respect to its production. This confirms the result of the morphological analysis in §5.2 that turbulence is not produced locally in the core by mergers at  $z < 0.15$ , but that it decays in this region. The impact of this turbulent dissipation on the local energy budget of the cluster core can be seen from the comparison of the energy contributions in Table 2. Similar to the global analysis in Table 1, there is a clear decrease of  $e_{\text{kin}}$ , transferred both to  $e_t$  and  $e_{\text{int}}$ . Both  $e_{\text{tot}}$  and  $e_{\text{int}}$  are higher in the FEARLESS run, pointing to the existence of an energy flux from the resolved scales to the thermal reservoir through the turbulent buffer, leading to the increase of the internal energy. We interpret this additional energy contribution as caused by the turbulent dissipation introduced by the SGS model.

In the cluster core, the energy content at the subgrid scales is marginal. Apparently the relative contribution to the total energy is even smaller than in Table 1, but one should notice that, for consistency, in that table both  $E_{\text{kin}}$  and  $E_t$  are reported according to the original scale separation introduced by the AMR resolution, and without rescaling  $E_t$  as described in §5.1. In the cluster core the refinement level is maximum, therefore the unresolved part of the turbulent cascade is relatively smaller than elsewhere, and so is  $e_t$ . In Table 2 we use the scaled definition of  $e_t$ , but in the core it differs from the unscaled one only marginally, because in this region the resolution is  $l_{\text{min}}$  almost everywhere.

To further quantitatively appreciate the contribution of  $e_t$  to the energy budget, Fig. 11 reports the profile of the turbulent pressure support  $p_t/(p_t + p_{\text{therm}})$  in the cluster, where the turbulent pressure is defined as  $p_t = 1/3 \rho q^2$ , and  $p_{\text{therm}}$  is the usual thermodynamical pressure. This ratio is also equal to the ratio of the corresponding energies ( $e_t/(e_t + e_{\text{int}})$ ). At the length scale of the effective spatial resolution of the simulations  $l_{\text{min}} = 7.8 \text{ kpc h}^{-1}$ , the contribution of the turbulent pressure (or energy) is well below 1%, although it increases at larger central distances.

In analogy with the turbulent pressure, we define a “resolved pressure”

$$p_{\text{res}} = \frac{1}{3} \rho v_{\text{rms}}^2, \quad (48)$$

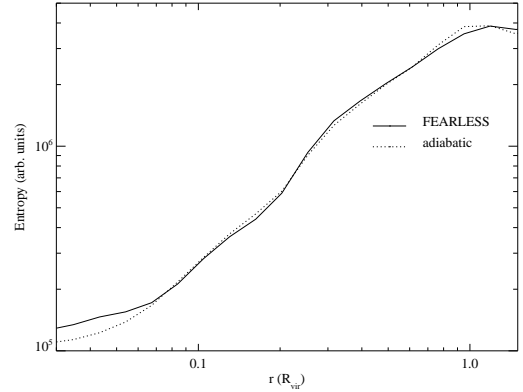


FIG. 12.— Same as Fig. 9, but showing the mass-weighted entropy (as defined in the text).

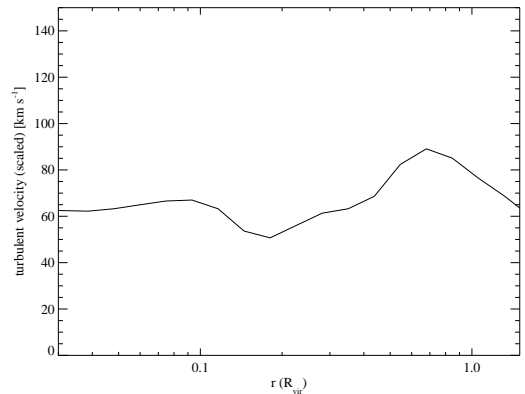


FIG. 13.— Radial profile of the turbulent energy scaled at the length scale  $l_{\text{min}}$ , as described in §4.2, for the FEARLESS simulation at  $z = 0$ .

where the root-mean-square (hereafter rms) velocity (Iapichino & Niemeyer 2008) is defined as

$$v_{\text{rms}} = \frac{\sum_i m_i (v_i - \langle v \rangle)^2}{\sum_i m_i}. \quad (49)$$

Here,  $\langle v \rangle$  is the mass-weighted average of the velocity in the analysis volume. This quantity essentially probes the contribution of turbulent motions at length scales of the order of  $0.07 R_{\text{vir}} \sim 90 \text{ kpc h}^{-1}$ . As shown in Table 2, the pressure contribution at these length scales is at the percent level, and is slightly higher in the FEARLESS simulation. Interestingly, the rms velocity in the FEARLESS run is also somewhat larger than in the adiabatic case.

The changes in the temperature and density profiles are also reflected on the entropy which is defined, as is customary in astrophysics, as

$$K = \frac{T}{\rho^{\gamma-1}} \quad (50)$$

with  $\gamma = 5/3$ . The entropy in the cluster core is higher in the FEARLESS run as compared to the standard run (Fig. 12). This result is consistent both with the locally increased dissipation of turbulent to internal energy provided by the SGS model and with the higher degree of mixing induced in the cluster core, shown by  $v_{\text{rms}}$  in Table 2.

The radial distribution of turbulent energy is displayed

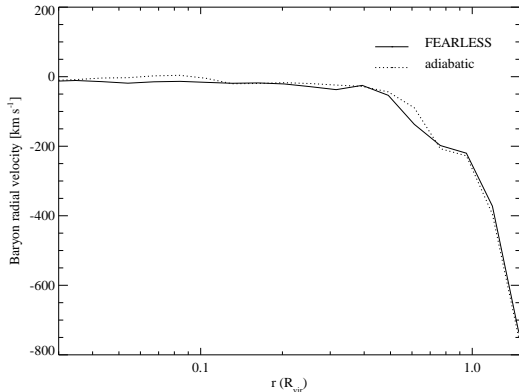


FIG. 14.— Same as Fig. 9, but showing the mass-weighted baryon radial velocity.

TABLE 3  
MASS-WEIGHTED AVERAGES IN A VOLUME OF  
[512 × 768 × 1280] kpc h<sup>-1</sup>, CONTAINING A SUBCLUMP  
AND ITS WAKE, AT z = 0.05.

Quantity	Adiabatic run	FEARLESS run
$\Sigma/\epsilon$	...	1.13
$e_{\text{tot}}$ [10 <sup>16</sup> cm <sup>2</sup> s <sup>-2</sup> ]	1.7447	1.5746
$e_{\text{int}}$ [10 <sup>15</sup> cm <sup>2</sup> s <sup>-2</sup> ]	5.4281	5.9607
$e_{\text{kin}}$ [10 <sup>16</sup> cm <sup>2</sup> s <sup>-2</sup> ]	1.2032	0.9786
$e_t$ [10 <sup>14</sup> cm <sup>2</sup> s <sup>-2</sup> ]	...	2.290
$p_t/(p_t + p_{\text{therm}})$ [%]	...	3.70

in Fig. 13 in terms of the turbulent velocity scaled to  $l_{\text{min}}$ . The turbulent velocity at this length scale is below 100 km s<sup>-1</sup>. There is a pronounced peak at  $r = 0.6 R_{\text{vir}}$  which is correlated with analogous trends in the turbulent pressure (Fig. 11) and in the radial velocity profile (Fig. 14). This structure is clearly linked with the most prominent merging clump shown in Fig. 8d, ed analysed below in Table 3.

There is an appealing similarity between the intervals of radii where  $q$  and the pressure ratio are larger ( $r < 0.1 R_{\text{vir}}$  and  $0.4 R_{\text{vir}} < r < 0.8 R_{\text{vir}}$ ), and the corresponding intervals where the temperature and entropy of the FEARLESS run are slightly larger than those computed for the adiabatic run. The opposite trend occurs in the interval in between, where  $v_{\text{turb}}$  is comparatively smaller. The effects are very small, but suggest that the SGS model plays the same role in the ICM that was shown above for the cluster core, and in §5.3 for the global quantities. In case of radial profiles, the spherical averaging combined with the intermittent behavior of turbulence tends to mask the turbulent effects. This can be better understood with a comparison of the values of  $q$  in Fig. 13 and in the right-hand panels of Figs. 7 and 8: the peak values in the slices are much larger than the spherical averages in the profile.

The idea that locally the turbulence and its modeling can play a sizeable role is further corroborated by the data in Table 3, reporting the analysis at  $z = 0.05$  of a small volume ( $512 \times 768 \times 1280$  kpc h<sup>-1</sup>) that contain one of the clumps presented in §5.2 and its wake (cf. Fig. 8a). The morphology of this accreting subcluster in the FEAR-

LESS run is not substantially different from the the adiabatic one. The energy content, however, is rather different from that in the cluster core: in the region under consideration  $e_{\text{kin}}$  is dominant with respect to  $e_{\text{int}}$ . The importance of the turbulence, injected by the hydrodynamical instabilities in the wake of the moving clump, is testified by the large ratio  $\Sigma/\epsilon$  and by the turbulent pressure support, which is at the level of some percent, about one order of magnitude larger than the spherical averages in Fig. 11. Despite of the slightly smaller average of  $e_{\text{tot}}$  in the FEARLESS run with respect to the adiabatic one, one can see an increase of  $e_{\text{int}}$ , mostly at the expenses of  $e_{\text{kin}}$ , resulting from the turbulent dissipation. The decrease of  $e_{\text{kin}}$  is rather large (19%) but can be partially ascribed to the difficulty of comparing energy budgets in such open volumes.

It is important to stress the deep difference between the turbulent velocity profile in Fig. 13 and the profile of  $v_{\text{rms}}$ , defined by equation (49) (see also Norman & Bryan 1999; Iapichino & Niemeyer 2008). In the former case, the mass-weighted average of a local quantity (i.e., defined in every cell) is computed for each spherical shell, whereas in the latter case  $v_{\text{rms}}$  is interpreted shell-wise as the standard deviation with respect to the average  $\langle v \rangle$ . Clearly, the latter definition does not retain any information related to a length scale, and can be interpreted as turbulent velocity only in a loose sense. From this point of view, the turbulent velocity provided by the SGS model is a more powerful probe of the features of a turbulent flow. On the other hand, spherically averaged velocity dispersions (and the derived turbulent pressure) are meaningful in comparison with observations, for example in the procedure for estimating the cluster mass (cf. Rasia et al. 2006). According to this different definition, the spherically averaged turbulent pressure of the simulated cluster (in a run similar to the adiabatic one presented here) is reported in Iapichino & Niemeyer (2008). It reaches values around 10%, in agreement with the values found recently in simulations by Lau et al. (2009) for relaxed clusters. The turbulent pressure is somewhat smaller in the FEARLESS run because of its slightly reduced content in kinetic energy, but the difference is small, and is not expected to significantly affect the estimates of the cluster mass.

## 6. DISCUSSION AND CONCLUSIONS

Large Eddy Simulations (LES) are based on the notion of filtering the fluid dynamic equations at a specific length scale, thus performing a scale separation between the resolved and the unresolved flow. The latter is treated by means of a subgrid scale model, which in turn is coupled to the hydrodynamical equations governing the former. In principle, a single scale separation is incompatible with adaptive mesh refinement (AMR) codes, often used to study astrophysical phenomena.

One of the aims of the present work was to address this numerical problem by means of developing, implementing, and applying a new numerical scheme that uses AMR and LES in combination, which we called FEARLESS. This novel tool is suitable for modeling turbulent flows over a wide range of length scales, a key feature in the treatment of many astrophysical flows including the intra-cluster medium.

We showed that the idea of our approach to cor-

rect the velocity and kinetic energy at grid refinement/derefinement, according to local Kolmogorov scaling, produces consistent results in simulations of driven turbulence. We demonstrated that energy conservation and the scaling of turbulent energy in our adaptive simulations is consistent with static grid simulations.

To our knowledge, this work shows the first application of an SGS model to simulations of the formation and evolution of a galaxy cluster. The results give rise to several interesting implications with regard to the physics of galaxy clusters and to the numerical methods employed for their exploration in computational cosmology.

The production of turbulence induced by minor mergers, analytically studied by Subramanian et al. (2006) and addressed by several numerical investigations (Heinz et al. 2003; Takizawa 2005a,b; Asai et al. 2007; Dursi & Pfrommer 2008; Iapichino et al. 2008), is accurately tracked by the newly defined turbulent subgrid energy (Figs. 7 and 8), although the level of resolution of the idealised setups cannot be reached by cosmological simulations. The visualization and subsequent analysis and postprocessing of turbulence and related quantities is therefore easier and more consistent. Turbulence in the ICM appears to be subsonic, in agreement with previous results. The average ratio between the dissipation and the production term  $\Sigma/\epsilon$  in the SGS model is close to unity, namely typical of a system where the turbulence is roughly stationary. On the other hand, this ratio is locally variable (cf. Table 2) and, together with the intermittent nature of turbulence in the ICM (§5.2; see also Iapichino & Niemeyer 2008), delivers the picture of a flow where turbulent motions are randomly initiated by merger events and then gradually decay (Frisch 1995; Subramanian et al. 2006). We also notice that, in simulations of driven turbulence in a periodic box (Fig. 3), the decrease of  $e_{\text{kin}}$  (noticed in our cluster simulation) is linked to an increase of  $e_t$  only in the early driving phase, not in the later equilibrium stage.

The morphological evolution of the minor merger events and the subsequent injection of turbulence in the ICM (Figs. 7 and 8) appear to be rather localized and intermittent, confirming the feature of turbulent flows as being not very volume-filling (Subramanian et al. 2006; Iapichino & Niemeyer 2008). The dissipation of turbulent to internal energy is thus modelled as a markedly local process, consistent with the theoretical expectations.

The effect of the SGS model on the cluster energy budget is well exemplified by the comparison of our simulations at  $z = 0$  (Table 1). Although the value of  $e_t$  is small compared to  $e_{\text{int}}$ , this energy buffer is locally effective in transferring the kinetic energy to the thermal component. The dissipative effects are therefore more relevant in those locations where  $e_t$  is relatively large, like the cluster core (Fig. 13). In general, the main contribution of the FEARLESS approach is to add a more physically motivated contribution to the energy dissipation, which in Eulerian codes is otherwise purely numerical. In FEARLESS, part of the energy flux from resolved scales to the thermal reservoir is retained in the buffer turbulent energy,  $e_t$ , and is further dissipated (turbulent dissipation) according to a local and temporal evolution determined by the SGS model.

Besides local effects, the importance of the SGS model for the overall cluster structure appears small, because of

the modest subgrid energy contribution (Fig. 11). One remark about the simulated cluster is important at this point: as also verified in Iapichino & Niemeyer (2008), this structure is very relaxed (see also Fig. 14). Simulations of more perturbed structures with recent or ongoing major mergers are in preparation (Paul et al. 2009), because they will help to clarify the role of the turbulent energy (and of its modelling) in the cluster energy budget in cases where its magnitude is larger. From this viewpoint, the radial increase of turbulent pressure support in the cluster outskirts (Fig. 11) is interesting for physical mechanisms (like the acceleration of cosmic rays and magnetic field amplification) where the knowledge of the turbulent state of the flow is needed.

More turbulence in the cluster core is required, for example, to reproduce the iron abundance profile in cool core clusters. Following Dennis & Chandran (2005), a turbulent diffusion coefficient can be defined as  $D_{\text{turb}} \sim 0.1 q l$ , where  $q$  is the turbulent velocity at the length scale  $l$ . Using  $l = l_{\text{min}}$  and  $q \sim 60 \text{ km s}^{-1}$ , we find  $D_{\text{turb}} \simeq 2 \times 10^{28} \text{ cm}^2 \text{ s}^{-1}$ . We notice that this value is smaller than the estimates of the effective diffusion coefficient in the cluster models of Rebusco et al. (2005) and Rebusco et al. (2006), which aim to reproduce the turbulent diffusion of metals in the cores of selected clusters. In particular, the cited models require much larger turbulent velocities. In the framework of our cluster simulation, these velocities could be injected into the ICM by a vigorous merger event. Another possibility, explicitly suggested by the authors cited above, is to invoke the action of an AGN outflow as an additional stirring agent in the cluster core.

The enhanced temperature profile in the FEARLESS run is somehow reminiscent of the theoretical predictions about the role of turbulent heating in cluster cores (Dennis & Chandran 2005). We notice an apparent misunderstanding in the literature regarding this point. In our model (and in the theory of turbulent flows in general), the dissipation of turbulent energy does not act as an additional energy source but simply releases the energy arising from the virialization process on a longer timescale than the quick shock heating. Nevertheless, we showed that turbulence, and the turbulent dissipation as well, can be rather localized. Naively, one could think that an effective turbulent heating in cool cores would require a peak of turbulent energy in the cluster core, whose existence and magnitude should be justified theoretically. Again, the stirring induced by AGN activity is an open possibility which deserves further investigation. However, the model of Dennis & Chandran (2005) includes radiative cooling and thermal conduction, and a detailed comparison is beyond the scope of the present work. We observe that additional physics which is here not addressed (thermal conduction, magnetic fields) could bring further interesting implications for the energy budget in the ICM and the turbulent mixing (Sharma et al. 2009, and references therein).

Consequent to both the enhanced dissipation and fluid mixing is the larger value of entropy in the FEARLESS cluster core. A long-standing problem in cluster simulations is the shape of the entropy profile, which smoothly decreases in the center in SPH simulations whereas it flattens inside the core in runs with grid-based codes (Frenk et al. 1999). This issue has been debated re-

cently in several works (among others, Dolag et al. 2005, Wadsley et al. 2008, Kawata et al. 2009), because it is controversial which difference of SPH and mesh-based codes it results from. It has been claimed that the source of discrepancy probably lies in the treatment of fluid mixing (Mitchell et al. 2009): the weaknesses of SPH in this regard are known, but the ability of mesh codes to model the turbulent cascade on length scales comparable with the grid resolution has not been addressed in a satisfactory way. It is therefore unclear whether the flat core entropy in grid codes correctly represents the physics of the ICM, or perhaps numerical effects harm the robustness of this feature. Recently, Springel (2009) pointed out that the core temperature and entropy in grid-based codes are affected by a spurious increase, caused by the N-body noise in the gravitational force field. In our opinion, the higher entropy core value in the FEARLESS run suggests that the typical flat entropy core is a hydrodynamical feature which requires a better understanding of the numerics in mesh codes, and is at least not primarily caused by N-body noise.

The SGS model applied in this work has to be considered as an intermediate solution to address some basic questions related to dynamics of the turbulent intra-cluster medium. A more elaborate model that

is able to handle the complexity of the flow (wide range of Mach numbers and large density gradients as well as pronounced inhomogeneities) in simulations of large scale structure evolution is under development (Schmidt & Federrath 2009). This first application shows the promising perspectives for the use of an SGS model in combination with AMR and its potential impact on many branches of numerical astrophysics.

L.I. acknowledges useful discussions with V. Antonuccio-Delogu, M. Bartelmann, S. Borgani, G. Murante, and M. Viel. The simulations described in this work were performed using the Enzo code, developed by the Laboratory for Computational Astrophysics at the University of California in San Diego (<http://lca.ucsd.edu>). We thank the Enzo development team, in particular D. Collins, for invaluable support in improving our modifications to the code. The numerical simulations were carried out on the SGI Altix 4700 *HLRB2* of the Leibniz Computing Centre in Munich (Germany). The research of J.C.N. and L.I. was partly supported by the Alfried Krupp Prize for Young University Teachers of the Alfried Krupp von Bohlen und Halbach Foundation.

#### REFERENCES

- Asai, N., Fukuda, N., & Matsumoto, R. 2007, *ApJ*, 663, 816  
 Berger, M. J., & Colella, P. 1989, *J. Comput. Phys.*, 82, 64  
 Berger, M. J., & Olinger, J. 1984, *Journal of Computational Physics*, 53, 484  
 Boussinesq, J. 1877, *Mem. Présentés par Divers Savants Acad. Sci. Inst. Fr.*, 23, 46  
 Bregman, J. N., & David, L. P. 1989, *ApJ*, 341, 49  
 Brüggem, M., Hoeft, M., & Ruszkowski, M. 2005, *ApJ*, 628, 153  
 Colella, P., & Woodward, P. R. 1984, *Journal of Computational Physics*, 54, 174  
 Deardorff, J. W. 1973, *ASME J. Fluids Engng.*, 429  
 Dennis, T. J., & Chandran, B. D. G. 2005, *ApJ*, 622, 205  
 Dolag, K., Vazza, F., Brunetti, G., & Tormen, G. 2005, *MNRAS*, 364, 753  
 Dursi, L. J., & Pfrommer, C. 2008, *ApJ*, 677, 993  
 Eisenstein, D. J., & Hu, W. 1999, *ApJ*, 511, 5  
 Eisenstein, D. J., & Hut, P. 1998, *ApJ*, 498, 137  
 Favre, A. 1969, *SIAM: Problems of hydrodynamics and continuum mechanics*, 231  
 Frenk, C. S., White, S. D. M., Bode, P., Bond, J. R., Bryan, G. L., Cen, R., Couchman, H. M. P., Evrard, A. E., Gnedin, N., Jenkins, A., Khokhlov, A. M., Klypin, A., Navarro, J. F., Norman, M. L., Ostriker, J. P., Owen, J. M., Pearce, F. R., Pen, U.-L., Steinmetz, M., Thomas, P. A., Villumsen, J. V., Wadsley, J. W., Warren, M. S., Xu, G., & Yepes, G. 1999, *ApJ*, 525, 554  
 Frisch, U. 1995, *Turbulence. The legacy of A.N. Kolmogorov* (Cambridge: Cambridge University Press)  
 Fujita, Y., Matsumoto, T., & Wada, K. 2004a, *ApJ*, 612, L9  
 Fujita, Y., Suzuki, T. K., & Wada, K. 2004b, *ApJ*, 600, 650  
 Fureby, C., Tabor, G., Weller, H. G., & Gosman, A. D. 1997, *Phys. Fluids*, 9, 3578  
 Germano, M. 1992, *Journal of Fluid Mechanics*, 238, 325  
 Heinz, S., Brüggem, M., Young, A., & Levesque, E. 2006, *MNRAS*, 373, L65  
 Heinz, S., Churazov, E., Forman, W., Jones, C., & Briel, U. G. 2003, *MNRAS*, 346, 13  
 Iapichino, L., Adamek, J., Schmidt, W., & Niemeyer, J. C. 2008, *MNRAS*, 388, 1079  
 Iapichino, L., & Niemeyer, J. C. 2008, *MNRAS*, 388, 1089  
 Inogamov, N. A., & Sunyaev, R. A. 2003, *Astronomy Letters*, 29, 791  
 Jones, T. W. 2008, in *ASP Conference Series*, Vol. 386, *Extragalactic Jets: Theory and Observation from Radio to Gamma Ray*, ed. T. Rector & D. De Young, 398, arXiv e-prints: 0708.2284  
 Kawata, D., Okamoto, T., Cen, R., & Gibson, B. K. 2009, ArXiv e-prints, 0902.4002  
 Kim, W.-T. 2007, *ApJ*, 667, L5  
 Kolmogorov, A. 1941, *Akademiia Nauk SSSR Doklady*, 30, 301  
 Lau, E. T., Kravtsov, A. V., & Nagai, D. 2009, ArXiv e-prints, 0903.4895  
 Lesieur, M., & Metais, O. 1996, *Annual Review of Fluid Mechanics*, 28, 45  
 Mitchell, N. L., McCarthy, I. G., Bower, R. G., Theuns, T., & Crain, R. A. 2009, *MNRAS*, 395, 180  
 Nagai, D., & Kravtsov, A. V. 2003, *ApJ*, 587, 514  
 Narayan, R., & Medvedev, M. V. 2001, *ApJ*, 562, L129  
 Niemeyer, J. C., & Hillebrandt, W. 1995, *ApJ*, 452, 769  
 Norman, M. L. 2005, in Plewa T., Linde T., Weirs V.G, eds, *Lecture Notes in Computational Science and Engineering*, Vol. 41, *Adaptive Mesh Refinement – Theory and Applications*. Springer, Berlin, New York, 413  
 Norman, M. L., & Bryan, G. L. 1999, in *Lecture Notes in Physics*, Berlin Springer Verlag, Vol. 530, *The Radio Galaxy Messier 87*, ed. H.-J. Röser & K. Meisenheimer, 106  
 O’Shea, B. W., Bryan, G., Bordner, J., Norman, M. L., Ab el, T., Harkness, R., & Kritsuk, A. 2005, in *Lecture Notes in Computational Science and Engineering*, Vol. 41, *Adaptive Mesh Refinement – Theory and Applications*, ed. T. Plewa, T. Linde, V.G. Weirs (Berlin; New York: Springer), 341  
 Ostriker, J. P. 1993, *ARA&A*, 31, 689  
 Paul, S., Iapichino, L., Miniati, F., Bagchi, J., & Mannheim, K. 2009, in preparation  
 Pope, E. C. D., Pittard, J. M., Hartquist, T. W., & Falle, S. A. E. G. 2008, *MNRAS*, 253  
 Rasia, E., Ettori, S., Moscardini, L., Mazzotta, P., Borgani, S., Dolag, K., Tormen, G., Cheng, L. M., & Diaferio, A. 2006, *MNRAS*, 369, 2013  
 Rebusco, P., Churazov, E., Böhringer, H., & Forman, W. 2005, *MNRAS*, 359, 1041  
 —. 2006, *MNRAS*, 372, 1840  
 Rebusco, P., Churazov, E., Sunyaev, R., & Böhringer, H. and Forman, W. 2008, *MNRAS*, 384, 1511  
 Reinecke, M., Hillebrandt, W., & Niemeyer, J. C. 2002, *A&A*, 391, 1167  
 Reynolds, C. S., McKernan, B., Fabian, A. C., Stone, J. M., & Vernaleo, J. C. 2005, *MNRAS*, 357, 242  
 Ricker, P. M., & Sarazin, C. L. 2001, *ApJ*, 561, 621  
 Roettiger, K., Loken, C., & Burns, J. O. 1997, *ApJS*, 109, 307  
 Röpke, F. K., & Hillebrandt, W. 2005, *A&A*, 431, 635

- Röpke, F. K., Hillebrandt, W., Schmidt, W., Niemeyer, J. C., Blinnikov, S. I., & Mazzali, P. A. 2007, *ApJ*, 668, 1132
- Röpke, F. K., & Schmidt, W. 2009, in *Lecture Notes in Physics*, Vol. 756, *Interdisciplinary Aspects of Turbulence*, ed. W. Hillebrandt & F. Kupka (Springer), 255–289
- Sagaut, P. 2006, *Large eddy simulation for incompressible flows an introduction* (Berlin: Springer-Verlag)
- Sarkar, S. 1992, *Physics of Fluids*, 4, 2674
- Scannapieco, E., & Brüggem, M. 2008, *ApJ*, 686, 927
- Schindler, S., & Mueller, E. 1993, *A&A*, 272, 137
- Schmidt, W. 2004, PhD thesis, Max-Planck-Institut für Astrophysics and Department of Physics, Technical University Munich
- Schmidt, W., & Federrath, C. 2009, in preparation
- Schmidt, W., Federrath, C., Hupp, M., Kern, S., & Niemeyer, J. C. 2009, *A&A*, 494, 127
- Schmidt, W., Niemeyer, J. C., & Hillebrandt, W. 2006, *A&A*, 450, 265
- Sharma, P., Chandran, B. D. G., Quataert, E., & Parrish, I. J. 2009, ArXiv e-prints, 0909.0270
- Shyy, W., & Krishnamurty, V. 1997, *Progress in Aerospace Sciences*, 33, 587
- Sijacki, D., & Springel, V. 2006, *MNRAS*, 366, 397
- Springel, V. 2009, ArXiv e-prints, 0901.4107
- Subramanian, K., Shukurov, A., & Haugen, N. E. L. 2006, *MNRAS*, 366, 1437
- Sunyaev, R. A., Norman, M. L., & Bryan, G. L. 2003, *Astronomy Letters*, 29, 783
- Takizawa, M. 2005a, *ApJ*, 629, 791
- Takizawa, M. 2005b, *Advances in Space Research*, 36, 626
- Wadsley, J. W., Veeravalli, G., & Couchman, H. M. P. 2008, *MNRAS*, 387, 427